Magnetic Resonance Materials in Physics, Biology and Medicine (2022) 35:719–732
https://doi.org/10.1007/s10334-021-00984-3

RESEARCH ARTICLE

Hemodynamics in a three-dimensional printed aortic model: a comparison of four-dimensional phase-contrast magnetic resonance and image-based computational fluid dynamics

Jieun Park[1] · Junghun Kim[2] · Sinjae Hyun[3] · Jongmin Lee[4]

Received: 20 May 2021 / Revised: 3 December 2021 / Accepted: 3 December 2021 / Published online: 8 February 2022

Abstract

Objective This study aims to compare an electrocardiogram (ECG)-gated four-dimensional (4D) phase-contrast (PC) magnetic resonance imaging (MRI) technique and computational fluid dynamics (CFD) using variables controlled in a laboratory environment to minimize bias factors.

Materials and methods Data from 4D PC-MRI were compared with computational fluid dynamics using steady and pulsatile flows at various inlet velocities. Anatomically realistic models for a normal aorta, a penetrating atherosclerotic ulcer, and an abdominal aortic aneurysm were constructed using a three-dimensional printer.

Results For the normal aorta model, the errors in the peak and the average velocities were within 5%. The peak velocities of the penetrating atherosclerotic ulcer and the abdominal aortic aneurysm models displayed a more extensive range of differences because of the high-speed and vortical fluid flows generated by the shape of the blood vessel. However, the average velocities revealed only relatively minor differences.

Conclusions This study compared the characteristics of PC-MRI and CFD through a phantom study that only included controllable experimental parameters. Based on these results, 4D PC-MRI and CFD are powerful tools for analyzing blood flow patterns in vivo. However, there is room for future developments to improve velocity measurement accuracy.

Keywords PC-MRI · Hemodynamics · Computational fluid dynamics · Abdominal aorta

Introduction

The hemodynamic properties of blood flow in blood vessels are closely related to the development of cardiovascular disease [1]. When hemodynamic forces on endothelial cells, such as pressure or frictional shear stress, change because of abnormal blood flow, they can cause inflammatory lesions that promote cardiovascular diseases such as atherosclerosis, aortic dissections, and aneurysms [2–5]. In addition, forces such as pressure on vessel walls directly affect the development of arteriosclerotic plaque and an increase in aneurysmal ruptures [6, 7]. Therefore, an analysis of hemodynamic factors in normal and patient groups can assist in the early diagnoses and prognoses of cardiovascular diseases [8].

Two-dimensional phase-contrast magnetic resonance imaging (2D PC- MRI) with one-directional velocity encoding is often used to generate images within a short time when evaluating hemodynamic information. However, to ensure accurate blood flow encoding, 2D PC-MRI requires that the examination area be perpendicular to the direction of the blood flow. Thus, the shapes of blood vessels were one limitation inhibiting the collection of blood flow information using this method [9]. More recently, a four-dimensional (4D) PC-MRI technique has been developed to overcome this limitation of 2D PC-MRI. 4D PC-MRI is a flow visualization technology that can measure three-dimensional (3D)

Jongmin Lee and Junghun Kim contributed equally to this article.

✉ Junghun Kim
fainal2@naver.com

✉ Jongmin Lee
jonglee@knu.ac.kr

[1] Nonlinear Dynamics Research Center, Kyungpook National University, Daegu, Republic of Korea

[2] Bio-Medical Research Institute, Kyungpook National University and Hospital, Daegu, Korea

[3] Department of Biomedical Engineering, Mercer University, Macon, GA 31207, USA

[4] Department of Radiology, Kyungpook National University and Hospital, 50, Sam-Duk 2 Ga, Jung Gu, Daegu 700-721, Republic of Korea

blood flow information by obtaining the orthogonal phase information of three-directional velocities. This imaging technique is appropriate for analyzing temporally varying hemodynamic information from blood vessels at various angles [10].

Furthermore, the vessel wall's cross-sectional area, average velocity, maximum velocity, and wall shear stress (WSS) acting on the vessel wall can be quantified within a specific region of the vessel [11]. The ability to visualize this information helps examine blood vessels with complex structures, by for example using streamlines to represent the flow of blood and using vector fields to represent the magnitude and direction of blood flow [12]. The 4D PC-MRI, which is quite sensitive to spatial resolution, needs a high-resolution scan to capture the flow of blood, which has a very complex flow pattern [13]. However, this technique is chiefly scanned at a lower resolution than the required resolution because the high-resolution scan can increase the scan time that may also cause an increase in patient discomfort and increased noise. Low-resolution images result in the loss of flow information regarding voxel velocity, partial volume effect, and inaccurate definitions of the vessel walls [14].

Computational fluid dynamics (CFD), a branch of fluid mechanics, is also applied to the cardiovascular system. CFD numerically solves complex fluids flowing within ducts of arbitrarily complex geometry with Navier–Stokes (NS) partial differential equations and is usually assisted by computer technology [15]. Combined with cardiovascular imaging, CFD simulation enables detailed characterization of complex flow fields which cannot be directly measured. The CFD model is currently being utilized as a clinical tool for physicians to treat coronary, valvular, congenital, myocardial and peripheral vascular diseases [16–20].

Research has now focused on diagnosing various diseases using 4D PC-MRI, and several research groups have conducted studies to verify the clinical usefulness of PC-MRI. For example, Cebral et al. [21] showed a good qualitative agreement between CFD and 4D PC-MRI in intracranial arteries. Boussel et al. [22] showed that velocity fields estimated by 4D PC-MRI are acceptable for clinical use but did not provide accurate measurements of WSS. Boccadifuoco et al. [23] showed a generally good qualitative agreement of MRI data with CFD for the velocity maps. Miyazaki et al. [24] investigated the aorta's flow rate, velocity, and WSS using 4D PC-MRI. Based on a comparison of these data gathered using computational fluid dynamics (CFD), the velocities obtained were correlated in the ascending aorta. However, the flow rate from 4D PC-MRI was underestimated, and the WSS values disagreed.

Cibis et al. [25] measured the WSS of the carotid artery using 4D PC-MRI. Compared with CFD, the pattern of WSS matched well, but the error rate of the WSS value was more than 30%. However, existing validation studies of 4D PC-MRI and CFD found differences due to the characteristics of the technique and external variables of the measurement object, such as breathing, motion of the object, and elasticity of blood vessels. These external variables may hamper the accurate quantification of hemodynamic characteristics obtained using the 4D PC-MRI technique and CFD by causing artifacts and errors. Therefore, it is desirable to quantify such validations by minimizing the external variables used to analyze the hemodynamic characteristics of aortic diseases. It is necessary to measure the velocity using the two techniques by acquiring and comparing the data through the phantom model, which can measure the actual area and monitor the actual volume passing through the phantom with a flowmeter. In addition, existing studies confirmed the usefulness of 4D PC-MRI with simple geometry [26, 27]. However, in the case of blood flow, which is affected by geometry, to increase clinical usefulness, it is necessary to verify the effect of 4D PC-MRI technology and CFD using a phantom including actual anatomical information of the human body.

This study focuses on comparing 4D PC-MRI and CFD based on phantom studies by controlling core variables and minimizing external variables such as breathing, motion, and vessel elasticity that could affect flow in laboratory settings. This study is composed of two parts. First, the average and maximum velocities of the phantom are measured by 4D PC-MRI under controlled, steady flow conditions and are then compared with CFD. Second, the average velocity, maximum velocity, WSS, and the streamlines of the phantom are measured by 4D PC-MRI under controlled pulsatile flow conditions and then compared with CFD.

Methods

When the blood flow measurement characteristics of 4D PC-MRI were evaluated, fluid flow was first investigated under steady conditions using physiological, penetrating atherosclerotic ulcer (PAU), and abdominal aortic aneurysm (AAA) models printed using a 3D printer. Then, the maximum velocity, average velocity, cross-sectional area, and flow rate were quantitatively analyzed in low- and high-speed steady flow environments before being compared with CFD treatments.

In the second experiment, the hemodynamic properties were investigated in a pulsatile flow environment using the same Normal, PAU, and AAA models created with the 3D printer to assess the blood flow measurement characteristics of 4D PC-MRI during pulsatile flow. The maximum velocity, average velocity, average flow rate, WSS, and streamlines were quantitatively and qualitatively analyzed and then compared with CFD.

Flow phantom and flow system

The phantom was constructed, and the flow system was configured to evaluate the accuracy of PC-MRI using only controlled variables to identify any PC-MRI problems in a laboratory environment. This model eliminated uncontrollable factors from the in vivo experimental measurements, such as breathing, movement, blood pressure, and vascular elasticity [28, 29].

Computed tomography (CT) data having a spatial resolution higher than MRI was acquired to produce the flow phantoms. CT data acquisition was performed at the Department of Radiology of the Kyungpook National University Hospital. The study was approved by the institutional review board (IRB) of the Kyungpook National University (KNU 2018-0175), and the IRB exempted consent from the patients, given that it was a retrospective study. Before further data processing, the CT data were anonymized.

A flow phantom was designed to validate the 4D PC-MRI. Specifically, 3D printed abdominal aorta models were created from clinical CT imaging data, which replicated the anatomic characteristics of aortic diseases. The process created 3D printed models of a physiological abdominal aorta, penetrating ulcer, and aneurysmal aortas from three patients. Subsequently, CT images were segmented using commercial software (ScanIP, Simpleware Ltd., Exeter, UK) and later used to reconstruct the vessels. CT scans were performed using a General Electric Revolution EVO (GE Healthcare, Milwaukee, WI, USA). The phantoms were created using a 3D printer (Project 7000, 3D Systems, USA), as shown in Fig. 1. An inelastic material Visijet SL Clear (3D Systems, USA), was used as the output material to produce a controllable phantom. To obtain a sufficient signal, thus a good SNR, the phantom was surrounded by agar at a concentration of 3%, equivalent to human tissue signal intensity for T1-weighted magnetic resonance (MR) scan images at 3.0 T [30]. The T1 and T2 value of agar at a concentration of 3% was 327 ± 4 ms and 34 ± 1 ms, respectively.

Each phantom vessel was connected to a pump that supplied either steady or pulsatile flows. In Fig. 2, the flow system is displayed. Note that 63% water and 37% glycerol were mixed to mimic human blood viscosity and density, and this fluid was supplied to the flow system [31, 32]. The T1 value of the mixed fluid was 1184 ± 54 ms.

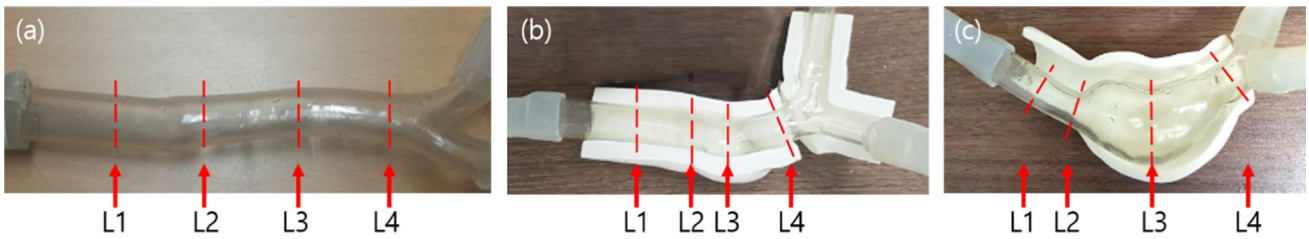

Fig. 1 Photograph of 3D printed phantom vessel designs. 3D printed abdominal aorta models were created from clinical CT imaging data, and these models replicated the anatomic characteristics of aortic diseases. The average velocity and peak velocity were measured at L1, L2, L3, and L4, respectively: (**a**) physiological, (**b**) PAU, and (**c**) AAA phantoms

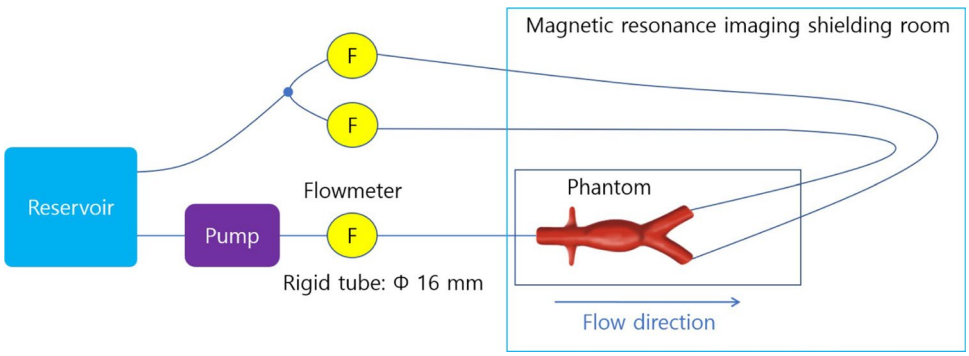

Fig. 2 Diagram of the flow system. Each phantom vessel was connected to a pump that supplies steady or pulsatile flows. Water and glycerol were mixed into a concentration of 6.3:3.7 to mimic human blood viscosity and density, and this fluid was provided to the flow system. The phantom supplied the flow by connecting a steady flow pump and a 16 mm inner-diameter polyvinyl chloride tube. An electromagnetic flowmeter was used to quantify the injection rate

Experiment 1: comparison between 4D PC-MRI and CFD using the abdominal aortic model with a steady flow

All image acquisitions were performed using a 36-channel receive body coil on a 3.0 T MR scanner (Discovery 750, GE Healthcare, Milwaukee, WI, USA). The 4D PC-MR sequence parameters were as follows: repetition time (TR) = 4.4–5.9 ms, echo time (TE) = 2.4–2.8 ms, velocity encoding (VENC) = 43–231 cm/s, views per segment (VPS) = 5–6, field of view (FOV) = 30 × 30 × 27 cm, slice thickness = 3 mm, flip angle = 8°, and bandwidth = 62.5 Hz/pixel. TR, TE, and VENC were determined based on the fluid velocity that was based on the Reynolds number (Re) (Table 1). The sequence was performed using 3D fast field echo phase-contrast during retrospective cardiac gating (20 frames per cycle). The 3D CINE data was acquired using interleaved four-point velocity encoding. The four 3D raw datasets were collected with a reference scan and three velocity-encoded acquisitions to measure three-directional blood flow velocities (*V*x, *V*y, and *V*z) in each cardiac phase. Within each heartbeat, a certain number of k-space lines were sampled for each frame. This number is called the views per segment (VPS). The time resolution (T_{res}) of such a 4D phase-contrast sequence is defined as follows: $T_{res} = 4 \times TR \times VPS$, where TR is the repetition time. Factor 4 is the result of the sequence design [33]. Gradients in the magnet field can create phase artifacts like eddy currents that cause blood flow values to be incorrect. In this study, the corrections for Maxwell phase effects and encoding errors related to gradient field distortions were performed, and the eddy current correction (ECC) was performed to correct background velocity offset.

Table 1 4D MRI scan parameters using steady flow

Scan parameters	Value
Surface coil	36-channel body coil
Repetition time (TR)	4.4–5.9 ms
Echo delay time (TE)	2.4–2.8 ms
Matrix size	200×200×90
Field of view (FOV)	30×30×27 cm
Slice thickness	3 mm
Flip angle	8°
Cardiac phase	20
Bandwidth	62.5 Hz/pixel
Velocity encoding (VENC)	43–231 cm/s

The fluid flow was maintained at steady flow conditions and corresponded to Reynolds numbers of 1000, 2000, 3000, and 4000 at the inlet, in which $Re = \frac{\rho v d}{\eta}$ where ρ, v, d, and η are density, velocity, diameter, and viscosity, respectively. The phantom supplied the flow via a steady flow pump and a 16 mm inner-diameter polyvinyl chloride (PVC) tube. An electromagnetic flowmeter (VMZ204, SIKA, Kaufungen, Germany) was used to check the injection rate.

Images acquired from 4D PC-MRI were analyzed using Arterys software (Arterys Inc., San Francisco, CA, USA). In Figure 1 shows the average and peak velocities measured at L1, L2, L3, and L4, respectively. The first experiment was to calibrate fluid flow. The coefficient of variation (CV) was calculated to assess the difference in flow rate based on the measurement level [34]. When the agreement between MRI and CFD was assessed, error percentages were calculated, and Bland–Altman plots were created for flow rate, area, average, and peak velocities for the normal aorta, PAU, and AAA.

ANSYS-CFX (ANSYS, Inc., USA) was used for the CFD simulation. For a comparison with 4D PC-MRI, ANSYS ICEM CFD (ANSYS, Inc., USA) imported the vessels reconstructed from CT and created the mesh (Fig. 3). The initial conditions were set the same to compare the two modalities. Specifically, the working fluid used in both setups had a density of 1083 kg/m^3 and viscosity of 0.0039 kg/(ms) at 20 °C.

The velocity profile measured in 4D PC-MRI was then assigned as the inlet boundary condition using equation (1), where u is the average velocity, u′ is the centerline velocity, r is the distance from the pipe axis, R is the radius, and n is a constant [35, 36]. The average and peak velocities were measured at the same location as for the 4D PC-MRI.

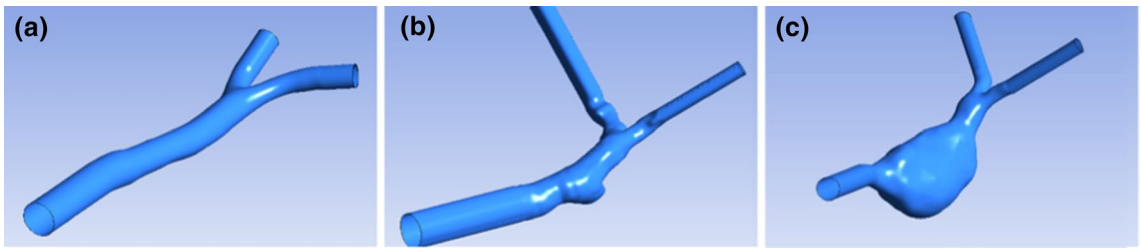

Fig. 3 CFD modeling. ANSYS-CFX was used to simulate the CFD. ANSYS ICEM CFD imported the vessels reconstructed from CT and created the mesh: (**a**) normal aorta, (**b**) PAU, and (**c**) AAA

$$\frac{u(r)}{u'} = \left(1 - \left(\frac{r}{R}\right)\right)^{\frac{1}{n}}. \quad (1)$$

Experiment 2: comparison between 4D PC-MRI and CFD using the abdominal aortic model with pulsatile flow

All measurements were performed using a 36-channel body coil on a 3.0T scanner (Signa Architect, GE Healthcare, Milwaukee, WI, USA). The 4D PC-MR sequence parameters were as follows: TR = 4.3–4.5 ms, TE = 2.3–2.4 ms, VENC = 157–296 cm/s, views per segment (VPS) = 5–6, FOV = 30 × 30 × 27 cm, slice thickness = 3 mm, flip angle = 8°, and bandwidth = 62.5 Hz/pixel. TR, TE, and VENC were determined based on the velocity of fluid using the pump settings, according to the motor's rotational speed (in beats per minute, BPM) (Table 2). The sequence was performed with 3D fast field echo-phase contrast during retrospective cardiac gating (20 frames per cycle).

Table 2 4D MRI scan parameters using pulsatile flow

Scan parameter	Value
Surface coil	36-channel body coil
Repetition time (TR)	4.3–4.5 ms
Echo delay time (TE)	2.3–2.4 ms
Matrix size	200×200×90
Field of view (FOV)	30×30×27 cm
Slice thickness	3 mm
Flip angle	8°
Cardiac phase	20
Bandwidth	62.5 Hz/pixel
Velocity encoding (VENC)	157–296 cm/s

The pulsatile flow was generated using a Harvard pump (Model 55-3305, Harvard Inc., Holliston, MA, USA), and the BPM settings were chosen to correspond to heart rates at 60 BPM and 70 BPM. The systole to diastole ratio was 5 to 5, and the stroke volume referred to the volume ejected per beat and was set to 80 ml. The pulsatile flow was supplied to the phantom using a 16 mm inner-diameter PVC tube connected to the Harvard pump. An electromagnetic flowmeter was then used to monitor the injection rate, and the images acquired from 4D PC-MRI were analyzed using CVI42 analysis software (Circle Cardiovascular Imaging, Calgary, Canada). In Fig. 4, the average velocity, peak velocity, flow rate, and WSS were measured at L1, L2, L3, L4, L5, and L6, respectively. Levels 5 and 6 in the second experiment, which can confirm the bifurcation characteristics, were measured as areas of interest because the human body has pulsatile flow. WSS can be obtained by multiplying the viscosity of the fluid by the local velocity gradient. The first step to measure WSS is to obtain the surface shape of the blood vessel from the blood vessel image acquired in the previous pre-processing step. From this, it is possible to extract the position of the vessel wall and the normal vector information at each position. Then, along the normal vector, the blood flow velocity near the vessel wall is extracted, and the blood flow gradient is calculated. As a result, the calculated velocity gradient is multiplied by the blood viscosity to obtain the WSS [8].

Fig. 5 shows the acquired 4D PC-MRI images to measure three-directional blood flow velocities and velocity maps according to measurement levels and various timings. The velocity vectors illustrate the streamline with vortices

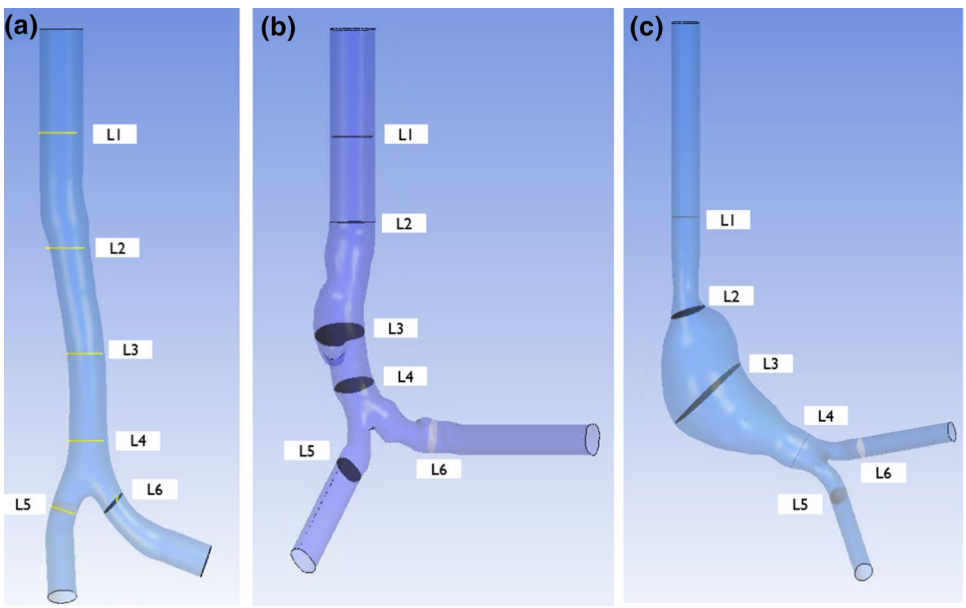

Fig. 4 4D PC-MRI measurement levels. The average velocity, peak velocity, average flow rate, and WSS were measured at L1, L2, L3, L4, L5, and L6, respectively: (**a**) normal aorta, (**b**) PAU, and (**c**) AAA

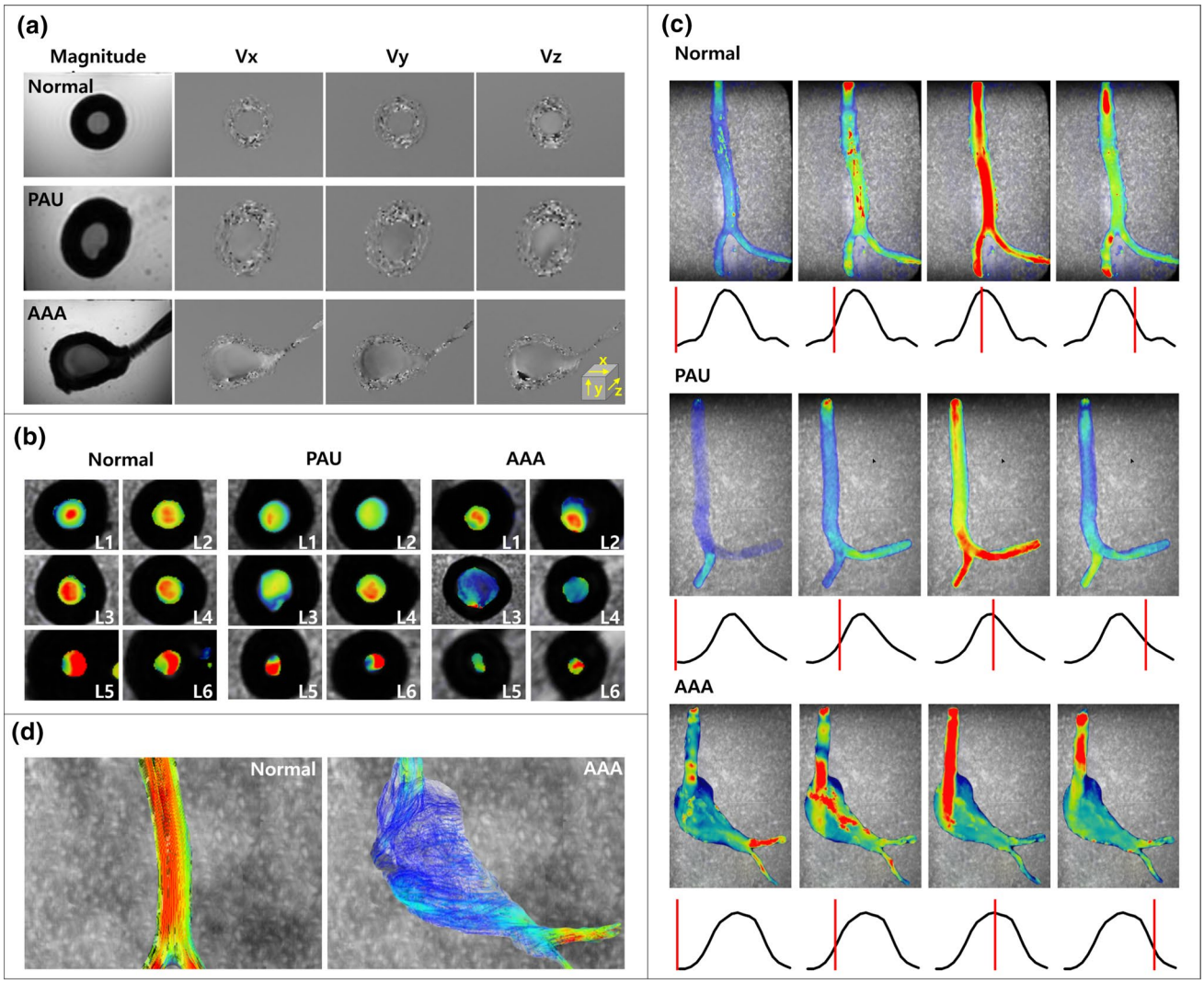

Fig. 5 Data acquisition and analysis image for 4D PC-MRI (**a**) The 4D PC-MRI images were collected to measure three-directional blood flow velocities (*V*x, *V*y, and *V*z) for each model. (**b**) The velocity map according to measurement levels. (**c**) The velocity at various timings of the pulsatile flow. (**d**) The streamline of the Normal model and AAA model

through the aneurysm in the AAA. There were large vortexes, and this was the main difference of flow characteristics in the Normal model and AAA model.

Group differences were assessed through a paired Student's t-test using normally distributed data. This analysis assessed the accuracy of PC-MRI obtained based on the controllable variables by minimizing external variables such as breathing, motion, and vessel elasticity. A Pearson's correlation coefficient was obtained using SPSS 20 (SPSS Inc., USA) between the CFD and the 4D PC-MRI data.

ANSYS-CFX was used to simulate the CFD, and ANSYS ICEM CFD imported the vessels reconstructed from the CT scans and created the mesh. The same experimental conditions as in the steady flow experiments were applied. In addition, the pulsatile inlet velocity profile measured using 4D PC-MRI was assigned as the inlet boundary condition. Furthermore, average velocity, peak velocity, average flow rate, and WSS were then measured at the same locations as those used for the 4D PC-MRI.

Results

Comparison between 4D PC-MRI and CFD using the abdominal aortic model during steady flow

Figure 6 shows the flow rate and area for positions L1, L2, L3, and L4 of the normal aorta (Normal), PAU, and AAA phantoms, as measured by 4D PC-MRI and CFD, at Reynolds numbers of 1000, 2000, 3000, and 4000. For

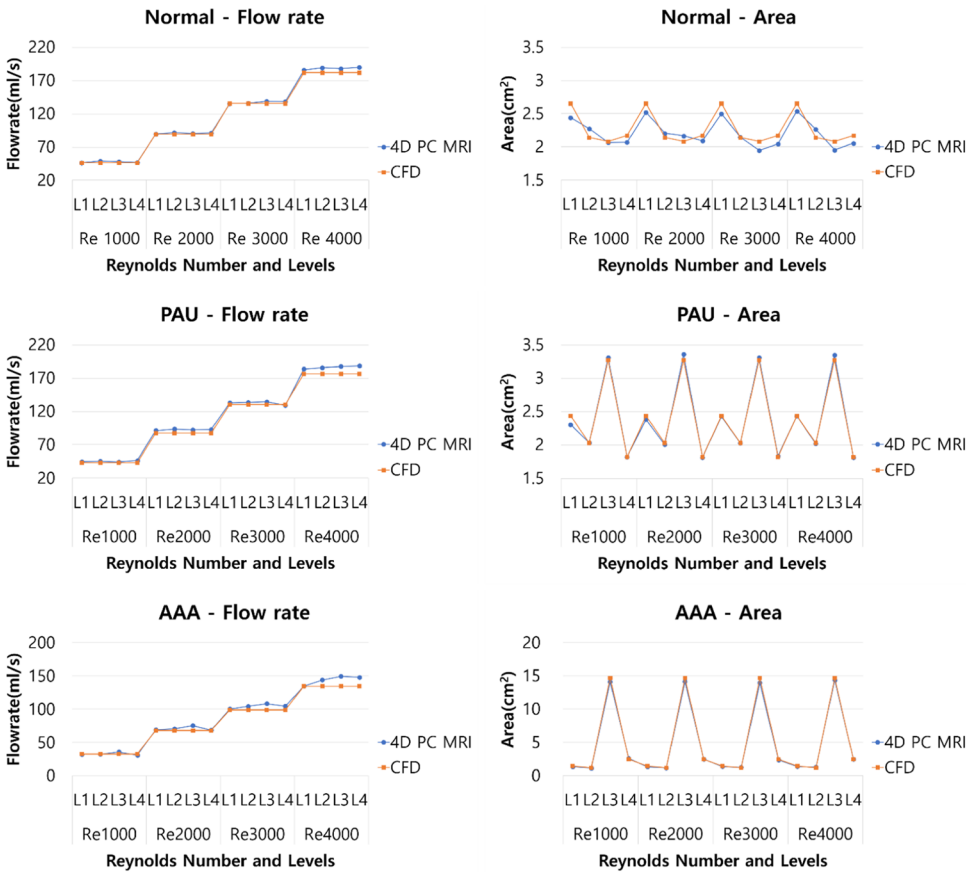

Fig. 6 Flow rate and area by level and Reynolds number, obtained using the two methods. The graph shows the flow rate and area for positions L1, L2, L3, and L4 of the normal aorta (Normal), PAU, and AAA models, as measured by 4D PC-MRI and CFD Reynolds numbers of 1000, 2000, 3000, and 4000

Table 3 CV of flow rate according to measurement level (L1, L2, L3, and L4) for each Reynolds number (Re)

Label	Re 1000 (%)	Re 2000 (%)	Re 3000 (%)	Re 4000 (%)
Normal CV	2	1	1	1
PAU CV	2	1	4	1
AAA CV	5	4	3	4

each model, the error percentages for the flow rate and each area were compared (4D PC-MRI vs. CFD). The error percentages were within 5%, on average. The CV was then calculated to evaluate any difference in the measurement level of the flow rate. As shown in Table 3, the CVs for the flow rate measurements at each level of 4D PC-MRI was approximately 5%.

Fig. 7 presents the average velocity and peak velocity at positions L1, L2, L3, and L4 for each constructed model, for Reynolds numbers 1000, 2000, 3000, and 4000. In the normal model, the error percentages for peak velocity and average velocity obtained using PC-MRI and CFD were within 5%, on average. For the PAU model, the error percentage for the average velocity for all Reynolds numbers and peak velocities when the Reynolds numbers were 1000 and 2000 were within 10%. However, for the Reynolds numbers of 3000 and 4000, the error percentages for the peak velocities were more than 10% at L3 and L4. In the AAA model, error percentages of the peak velocities differed by approximately 40% or more in some levels, and the average velocities' error percentages were approximately 15%. For the Normal model, peak velocity was higher in 4D PC-MRI than in CFD except for L1. For the PAU model, peak velocity was higher in 4D PC-MRI than in CFD except for L1 of all the Reynolds numbers and L2 of the Reynolds numbers 1000 and 2000. For the AAA model, peak velocity showed different results with higher values for each measurement level and did not show a constant trend.

The Bland-Altman analysis for these three models confirmed that the differences in peak velocities of PAU and AAA models tended to be greater in the normal model. For the Normal, PAU, and AAA models shown in Fig. 8, the bias and 95% limits of agreement (average bias ±2 SD) of the flow rates were − 2.35 ± 2.57 ml/s, − 4.66 ± 3.48 ml/s, and − 4.57 ± 5.18 ml/s; the areas were 0.09 ± 0.06 cm^2, 0.002 ± 0.04 cm^2, and 0.15 ± 0.25 cm^2; the average velocities were − 2.98 ± 2.47 cm/s, − 1.57 ± 1.38 cm/s, − 2.23 ± 2.13 cm/s; and the peak velocities were 0.38 ± 2.7, 4.84 ± 8.76, 6.31 ± 20.4 cm/s.

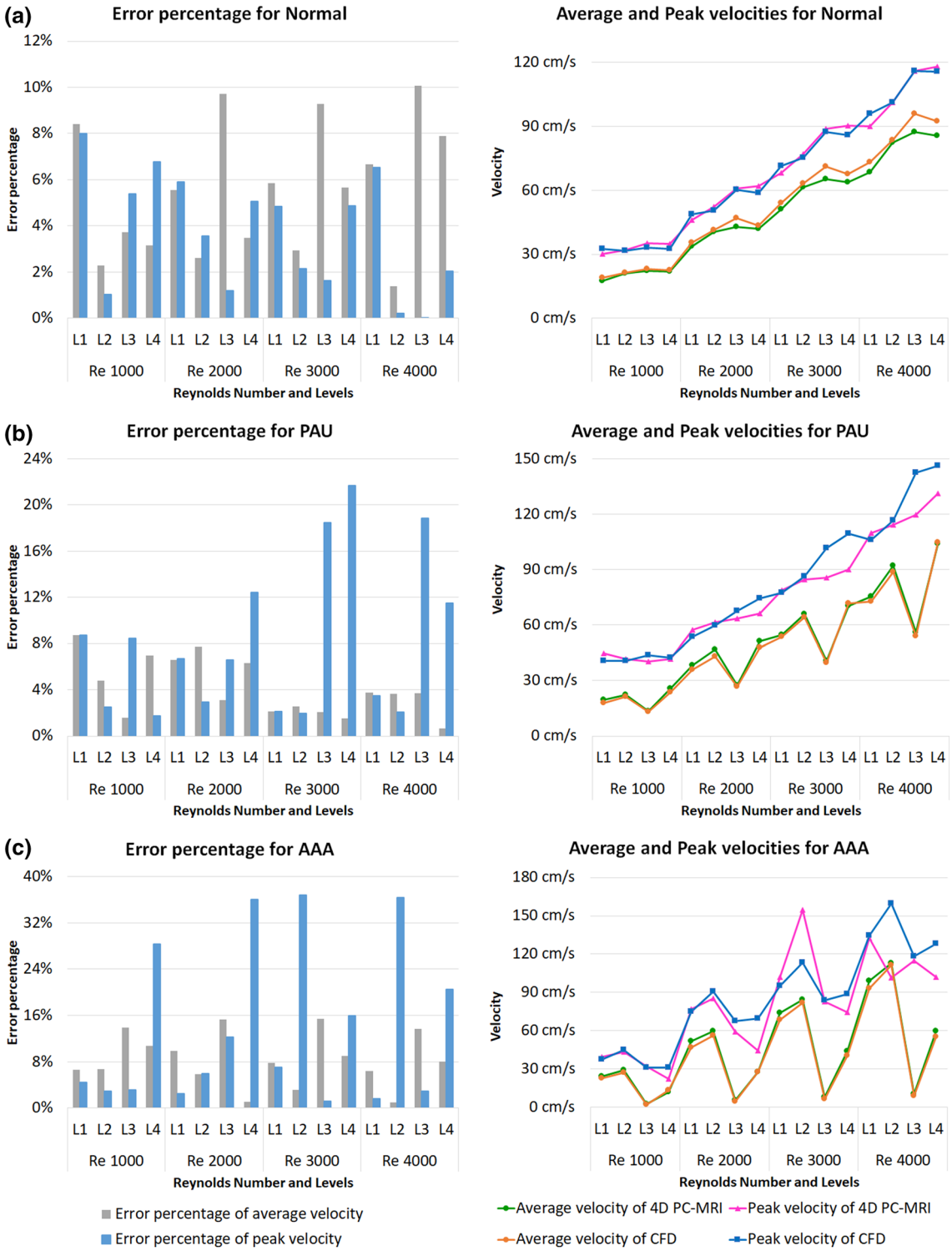

Fig. 7 Error percentages between 4D PC-MRI and CFD for average and peak velocities. The graphs show the average and peak velocities at positions L1, L2, L3, and L4 for each model at Reynolds numbers 1000, 2000, 3000, and 4000. (**a**) In the Normal model, the percentage error differences for the peak and average velocities estimated using PC-MRI and CFD were within 10%. (**b**) In the PAU model, the percentage error differences for the average velocities were within 10%. However, error percentages for peak velocities increased to more than 10% at L3 and L4 when the Reynolds numbers were 3000 and 4000. (**c**) In contrast, the error percentages of the peak velocities differed by approximately 40% or more in the AAA model. However, the error percentage for the average velocity was approximately 15%

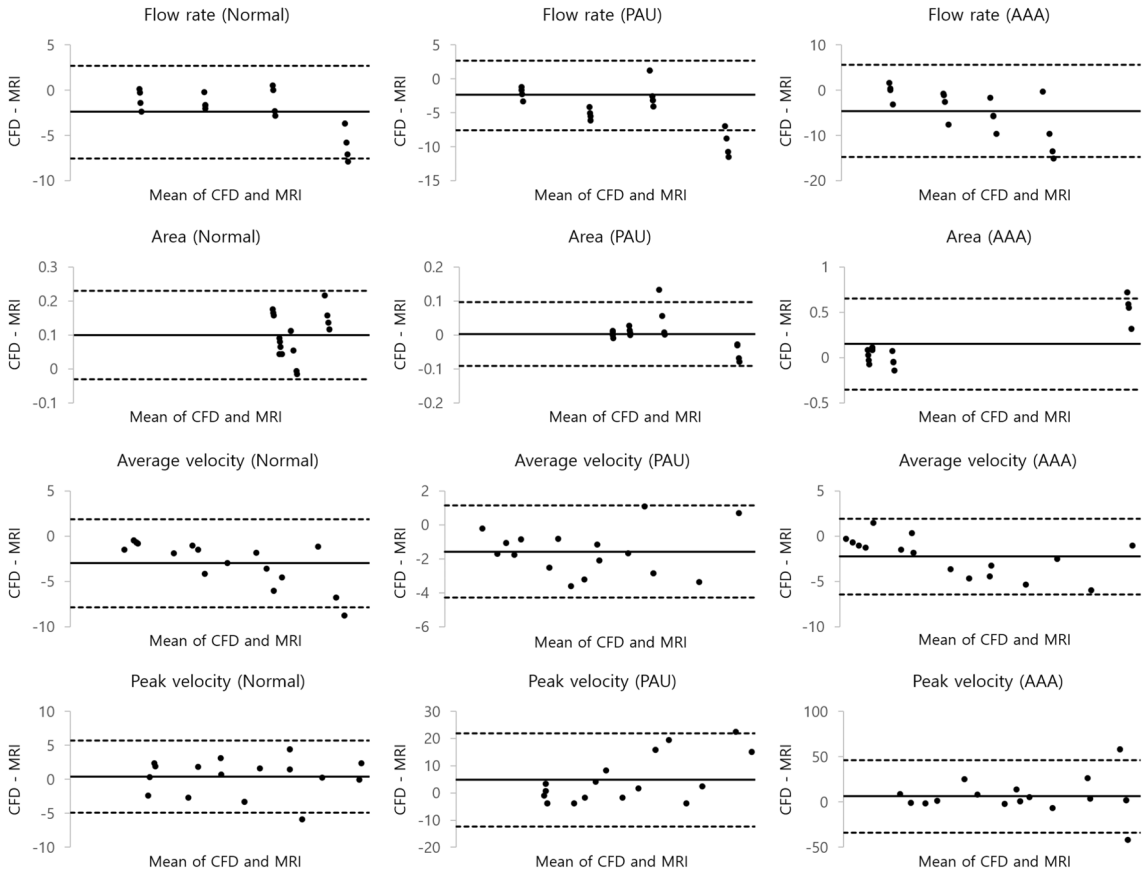

Fig. 8 To assess the agreement between MRI and CFD, Bland–Altman plots were created for the following: flow rate, area, average, and peak velocities for the Normal, PAU, and AAA models. For the Normal, PAU and AAA models, the bias and 95% limits of agreement (average bias ± 2 SD) of the flow rates were -2.35 ± 2.57 ml/s,— 4.66 ± 3.48 ml/s, and − 4.57 ± 5.18 ml/s; the areas were 0.09 ± 0.06 cm^2, 0.002 ± 0.04 cm^2, and 0.15 ± 0.25 cm^2; the average velocities were − 2.98 ± 2.47, − 1.57 ± 1.38, and − 2.23 ± 2.13 cm/s; and the peak velocities were 0.38 ± 2.7 cm/s, 4.84 ± 8.76 cm/s, and 6.31 ± 20.4 cm/s

Comparison between 4D PC-MRI and CFD using the abdominal aortic model during pulsatile flow

Fig. 9 shows the plots of average velocity measured at L1, L2, L3, L4, L5, and L6 for the Normal, PAU, and AAA models when the Harvard pump was operated at 60 BPM and 70 BPM, respectively. The peak velocity, average velocity, average flow rate, and WSS were obtained using both 4D PC-MRI and CFD.

The Normal and the PAU models displayed no significant differences in average velocity and flow rate, but significant differences were observed in the AAA model. Peak velocity and WSS showed significant differences compared to the average velocity and flow rate. Specifically, there were significant differences at many levels of the AAA model (Fig. 10). The Normal and PAU models revealed high correlations in the average velocity, peak velocity, flow rate, and WSS, with values being less than 0.5 at many levels of the AAA model (Fig. 11).

Fig. 12 presents the streamlines created by 4D PC-MRI and CFD. From these experiments, it was confirmed that the spatial patterns were similar, as it can be observed that the velocities in the bifurcation regions were high in all models. However, the velocity in the AAA model was significantly low in the region before branching compared to the Normal and PAU models. The helical flow patterns were also matched within the aneurysmal area in the AAA model.

Discussion

Blood flow affects endothelial cells and may result in pathogenesis, such as atherosclerosis. Thus, the ability to evaluate the hemodynamics of blood flow can be useful in diagnosing and treating vascular diseases, including blood vessel blockages and aneurysm ruptures. By analyzing blood flow, data from PC-MRI can provide valuable

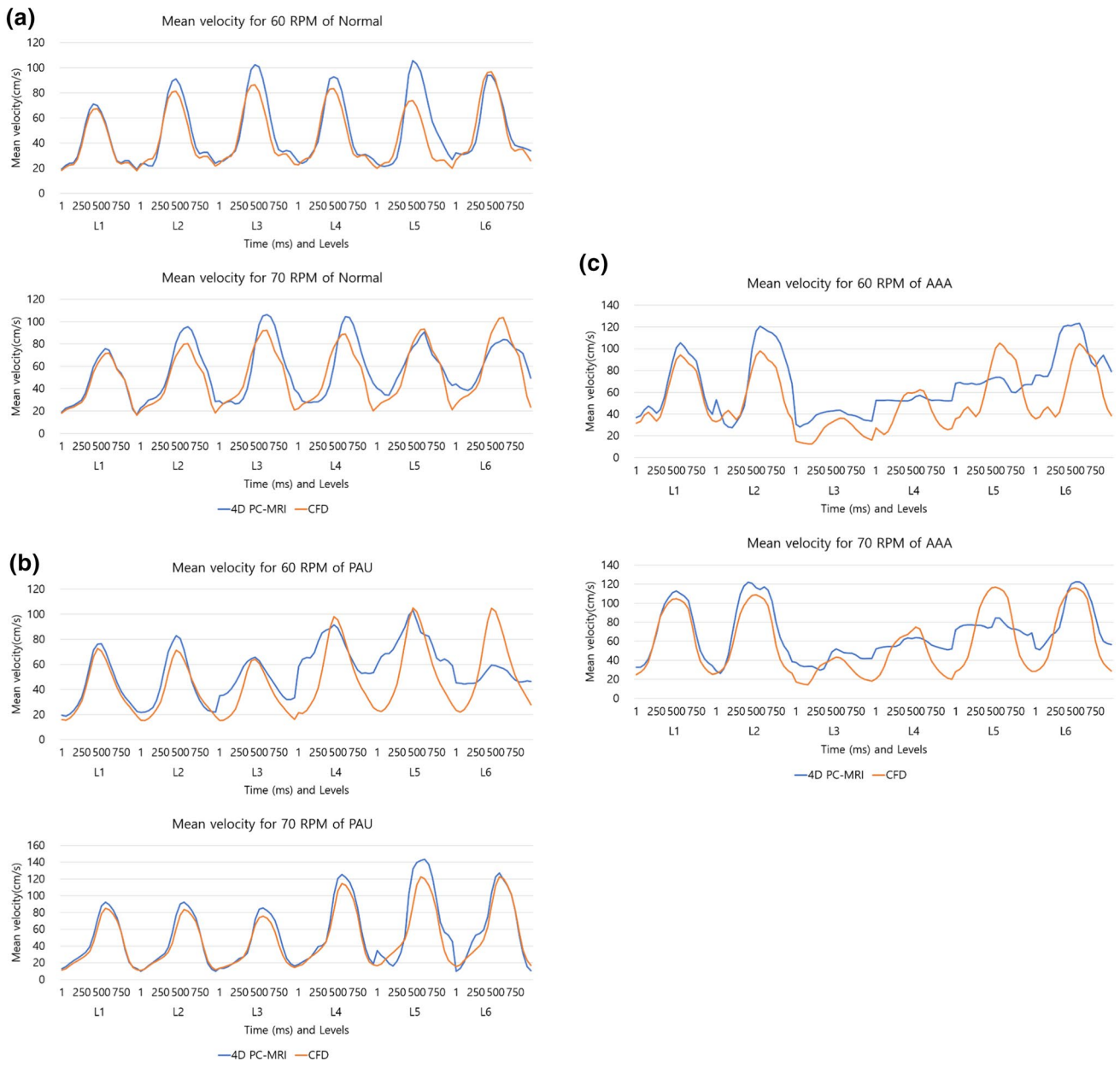

Fig. 9 Velocity curves as a function of time for measurements obtained using 4D PC-MRI and CFD. The graph shows the mean velocities measured at L1, L2, L3, L4, L5, and L6 for the Normal, PAU, and AAA models when the Harvard pump was operated at 60 BPM and 70 BPM: (**a**) Normal, (**b**) PAU, and (**c**) AAA models

information about the disease severity and provide support for treatment choices [37]. However, PC-MRI has been a traditionally powerful tool for analyzing blood flow in vivo but has been insensitive in measuring the velocity of a nonsteady flow, which is a characteristic of in vivo blood flow. It is essential to identify the exact hemodynamic characteristics of the PC-MRI data to analyze the blood flow. Studies attempting to quantify flow turbulence have recently been conducted in vascular diseases such as vascular stenosis and aneurysmal rupture. Other researches were done on technology that calculates the WSS, closely related to cardiovascular diseases, affecting vascular endothelial function [38, 39]. CFD can provide additional insights at a significantly higher spatial and temporal resolution to MRI. However, CFD requires an accurate definition of boundary conditions for geometry and physiology, and the reliable result depends on the precision of the boundary conditions [40].

The focus of this study was to verify the usefulness of PC-MRI for use in fluid flow measurements. Problems with these measurements include various bias factors, such as irregular heartbeats and the varied shapes of blood vessels

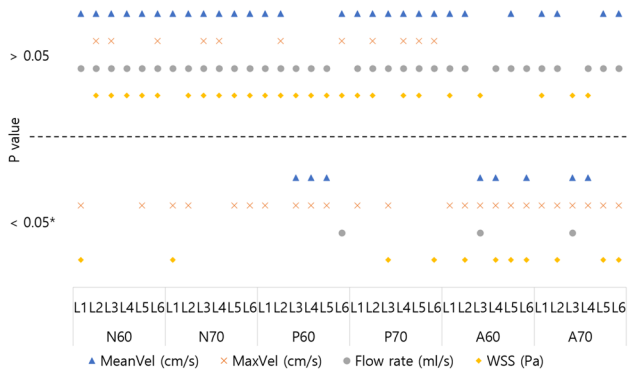

Fig. 10 The graph shows p values for mean velocity (MeanVel), maximum velocity (MaxVel), flow rate, and WSS between 4D PC-MRI and CFD. Asterisks indicate significantly different values between these groups ($p < 0.05$). Not significant (> 0.05). N60; Normal 60 BPM, N70; Normal 70 BPM, P60; PAU 60 BPM, P70; PAU 70 BPM, A60; AAA 60 BPM, A70; AAA 70 BPM

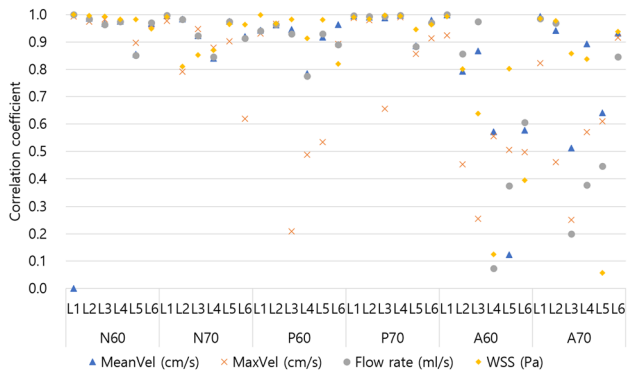

Fig. 11 Correlation coefficients for pairwise biomarker comparisons between 4D PC-MRI and CFD. The graph shows p values for mean velocity (MeanVel), maximum velocity (MaxVel), flow rate, and WSS. Specifically, the correlation between 4D PC-MRI and CFD for Normal and PAU is high, while it is relatively low at 60 BPM and 70 BPM for AAA. N60; Normal 60 BPM, N70; Normal 70 BPM, P60; PAU 60 BPM, P70; PAU 70 BPM, A60; AAA 60 BPM, A70; AAA 70 BPM

in the human body. The effects of these differences on the verification of PC-MRI remain uncertain, and, therefore, they are unreliable. Here, the study has measured the characteristics of 4D PC-MRI, minimizing the number of bias factors using a phantom model and compared with CFD.

The 4D PC-MRI was compared with CFD in the first experiments, using the abdominal aortic model based on CT data under a steady flow. As a result, the difference between CFD data and 4D PC-MRI was found to differ as a function of the blood vessel's shape. The difference was low in the Normal, having no turbulence. The AAA models had strong turbulence, while the PAU model had relatively light turbulence. Yet, errors associated with the peak velocity data of the region where turbulence occurred during high-speed flow conditions increased at higher Reynolds numbers. Importantly, it became difficult to trust the 4D PC-MRI data because the peak velocity error was prominent in regions where heavy turbulence occurs, such as in the AAA model. However, the average velocity appeared to display a relatively small error. Thus, the average velocity is more appropriate for reference rather than the peak velocity in clinical practice.

In the second experiment, the characteristics of 4D PC-MRI during a pulsatile flow were identified using the abdominal aortic model. For comparison purposes, the initial conditions were set to match those of CFD. When there was no turbulence, the correlation was high. However, the correlation was seen to be affected by the shape of the blood vessel. Therefore, the credibility of the velocity data was again challenged. Nevertheless, when the streamlines were visualized, features such as the velocity distribution and turbulence appeared similar. These findings are similar to those reported in published studies [25, 41, 42]. Ngo et al. [41] reported that the 3D blood flow visualization, secondary flows, and recirculation regions were of poorer quality when visualized through the 4D flow MRI. Kweon et al. [42] reported 4D PC-MRI accurately measures the flow rate in axial scans. However, there was a poor agreement for peak velocity between the 4D PC-MRI and CFD.

Velocity measurement using 4D PC-MRI is based on the principle of averaging the velocities within a voxel, which mainly results in limited spatial resolution and inaccuracies due to turbulent flow, thus resulting in loss of definition of complex flow patterns relative to the high resolution of CFD [21, 43]. Aneurysm or irregularly shaped vessels may yield worse results than relatively straight vessels [44]. In addition, if the velocity is significantly lowered due to an increase in the cross-sectional area, such as an aneurysm, the reliability is lower than the velocity close to the set Venc [45].

This study differs from actual elastic blood vessel investigations wherein a nonelastic phantom was used to minimize the number of variables that may affect the research results. However, as a result of this study (i.e., with the exclusion of the elastic variable), it was confirmed that the differences were large when turbulence occurred. Therefore, it must be considered that larger differences may occur when measuring actual blood vessel models that can make not only effect by the flow but also artifacts by the motion of blood vessels.

In conclusion, this study analyzed and compared 4D PC-MRI and CFD characteristics under well-controlled and idealized conditions. In the absence of a turbulent flow, 4D PC-MRI showed a strong linear relationship with CFD. However, the correlation grew weaker when considering specific geometries and degrees of turbulence. Furthermore,

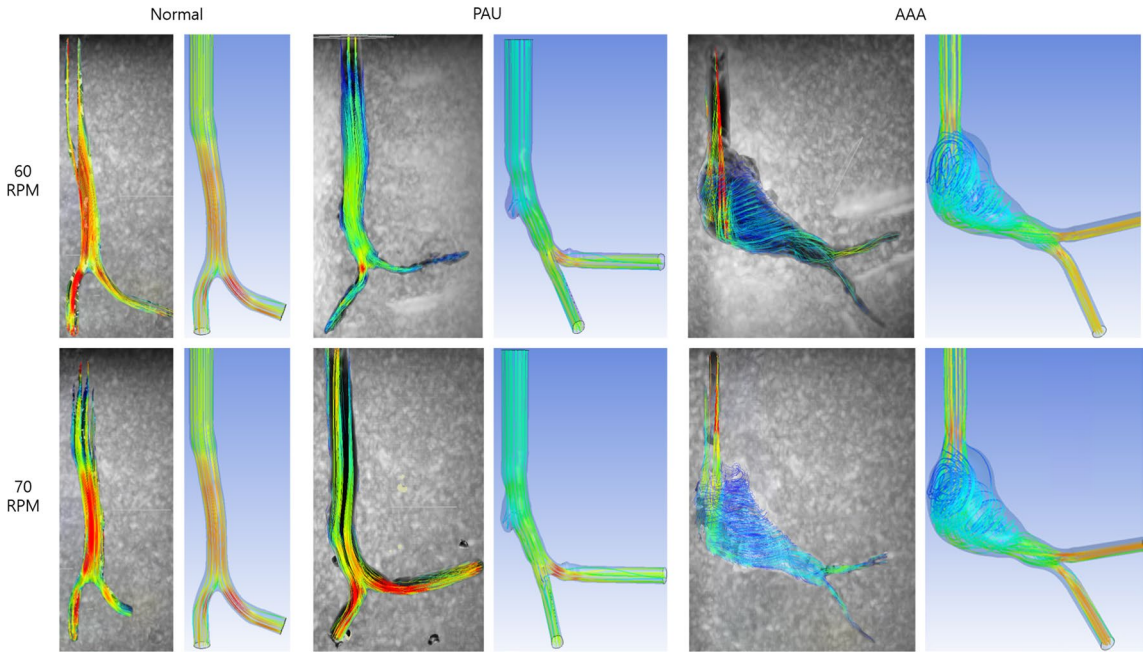

Fig. 12 Streamlines obtained from 4D PC-MRI and CFD. The figure shows the streamlines created by 4D PC-MRI and CFD. It is confirmed that similar patterns are obtained by each method

the velocity estimation of 4D PC-MRI depended on vessel shape, blood flow pattern, and the generation of turbulence, leading to inaccurate results. The streamline might be generally reliable by providing only global flow information—but not for the direct estimation of WSS and maximum velocity.

Funding This research received no specific grant from any funding agency in the public, commercial, or not-for-profit sectors.

Declarations

Conflict of interest No potential conflict of interest was reported by the authors.

Ethical approval All procedures performed in studies involving human participants were in accordance with the ethical standards of the institutional and national research committee and with the 1964 Helsinki declaration and its later amendments or comparable ethical standards.

Informed consent The study was approved by the institutional review board (IRB) of the Kyungpook National University (KNU 2018-0175), and the IRB exempted consent from the patients, given that it was a retrospective study.

References

1. Fisher AB, Chien S, Barakat AI, Nerem RM (2001) Endothelial cellular response to altered shear stress. Am J Physiol Lung Cell Mol Physiol 281(3):L529–L533. https://doi.org/10.1152/ajplung.2001.281.3.L529
2. Ku DN, Giddens DP, Zarins CK, Glagov S (1985) Pulsatile flow and atherosclerosis in the human carotid bifurcation. Positive correlation between plaque location and low oscillating shear stress. Arteriosclerosis 5(3):293–302. https://doi.org/10.1161/01.ATV.5.3.293
3. Barker AJ, Markl M, Bürk J, Lorenz R, Bock J, Bauer S, Schulz-Menger J, von Knobelsdorff-Brenkenhoff F (2012) Bicuspid aortic valve is associated with altered wall shear stress in the ascending aorta. Circ Cardiovasc Imaging 5(4):457–466. https://doi.org/10.1161/CIRCIMAGING.112.973370
4. Bissell MM, Hess AT, Biasiolli L, Glaze SJ, Loudon M, Pitcher A, Davis A, Prendergast B, Markl M, Barker AJ, Neubauer S, Myerson SG (2013) Aortic dilation in bicuspid aortic valve disease: flow pattern is a major contributor and differs with valve fusion type. Circ Cardiovasc Imaging 6(4):499–507. https://doi.org/10.1161/CIRCIMAGING.113.000528
5. Uretsky S, Gillam LD (2014) Nature versus nurture in bicuspid aortic valve aortopathy: more evidence that altered hemodynamics may play a role. Circulation 129(6):622–624. https://doi.org/10.1161/CIRCULATIONAHA.113.007282
6. Slager CJ, Wentzel JJ, Gijsen FJH, Thury A, van der Wal AC, Schaar JA, Serruys PW (2005) The role of shear stress in the destabilization of vulnerable plaques and related therapeutic implications. Nat Rev Cardiol 2:456–464. https://doi.org/10.1038/ncpcardio0298
7. Groen HC, Gijsen FJH, van der Lugt A, Ferguson MS, Hatsukami TS, van der Steen AFW, Yuan C, Wentzel JJ (2007) Plaque rupture in the carotid artery is localized at the high shear stress region: a case report. Stroke 38:2379–2381. https://doi.org/10.1161/STROKEAHA.107.484766
8. Ha H, Huh H, Yang DH, Kim N (2019) Quantification of hemodynamic parameters using four-dimensional flow MRI. J Korean Soc Radiol 80:239–258. https://doi.org/10.3348/jksr.2019.80.2.239
9. Bollache E, van Ooij P, Powell A, Carr J, Markl M, Barker AJ (2016) Comparison of 4D flow and 2D velocity-encoded phase

contrast MRI sequences for the evaluation of aortic hemodynamics. Int J Cardiovasc Imaging 32(10):1529–1541. https://doi.org/10.1007/s10554-016-0938-5
10. Stalder AF, Russe MF, Frydrychowicz A, Bock J, Hennig J, Markl M (2008) Quantitative 2D and 3D phase contrast MRI: optimized analysis of blood flow and vessel wall parameters. Magn Reson Med 60(5):1218–1231. https://doi.org/10.1002/mrm.21778
11. Pereira VM, Brina O, Bijlenga P, Bouillot P, Narata AP, Schaller K, Lovblad K-O, Ouared R (2014) Wall shear stress distribution of small aneurysms prone to rupture: a case-control study. Stroke 45:261–264. https://doi.org/10.1161/STROKEAHA.113.003247
12. Morbiducci U, Ponzini R, Rizzo G, Cadioli M, Esposito A, De Cobelli F, Del Maschio A, Montevecchi FM, Redaelli A (2009) In vivo quantification of helical blood flow in human aorta by time-resolved three-dimensional cine phase contrast magnetic resonance imaging. Ann Biomed Eng 37:516–531. https://doi.org/10.1007/s10439-008-9609-6
13. Kecskemeti S, Johnson K, Wu Y, Mistretta C, Turski P, Wieben O (2012) High resolution three-dimensional cine phase contrast MRI of small intracranial aneurysms using a stack of stars *k*-space trajectory. J Magn Reson Imaging 35(3):518–527. https://doi.org/10.1002/jmri.23501
14. Petersson S, Dyverfeldt P, Gårdhagen R, Karlsson M, Ebbers T (2010) Simulation of phase-contrast MRI intravoxel velocity standard deviation (IVSD) mapping. Magn Reson Med 64(4):1039–1046. https://doi.org/10.1002/mrm.22494
15. Zawawi MH, Saleha A, Salwa A, Hassan NH, Zahari NM, Ramli MZ, Muda ZC (2018) A review: fundamentals of computational fluid dynamics (CFD). AIP Conf Proc 2030(1):020252. https://doi.org/10.1063/1.5066893
16. Morris PD, van de Vosse FN, Lawford PV, Hose DR, Gunn JP (2015) "Virtual" (computed) fractional flow reserve: current challenges and limitations. JACC Cardiovasc Interv 8(8):1009–1017. https://doi.org/10.1016/j.jcin.2015.04.006
17. Simon HA, Ge L, Sotiropoulos F, Yoganathan AP (2010) Simulation of the three-dimensional hinge flow fields of a bileaflet mechanical heart valve under aortic conditions. Ann Biomed Eng 38:841–853. https://doi.org/10.1007/s10439-009-9857-0
18. Pennati G, Corsini C, Hsia T-Y, Migliavacca F, for the Modeling of Congenital Hearts Alliance (MOCHA) Investigators (2013) Computational fluid dynamics models and congenital heart diseases. Front Pediatr 1:4. https://doi.org/10.3389/fped.2013.00004
19. Chiu W-C, Girdhar G, Xenos M, Alemu Y, Soares JS, Einav S, Slepian M, Bluestein D (2014) Thromboresistance comparison of the HeartMate II ventricular assist device with the device thrombogenicity emulationoptimized HeartAssist 5 VAD. J Biomech Eng 136(2):021014. https://doi.org/10.1115/1.4026254
20. Dong J, Wong KKL, Tu J (2013) Hemodynamics analysis of patient-specific carotid bifurcation: a CFD model of downstream peripheral vascular impedance. Int J Numer Method Biomed Eng 29(4):476–491. https://doi.org/10.1002/cnm.2529
21. Cebral JR, Putman CM, Alley MT, Hope T, Bammer R, Calamante F (2009) Hemodynamics in normal cerebral arteries: qualitative comparison of 4D phase-contrast magnetic resonance and image-based computational fluid dynamics. J Eng Math 64(4):367–378. https://doi.org/10.1007/s10665-009-9266-2
22. Boussel L, Rayz V, Martin A, Acevedo-Bolton G, Lawton MT, Higashida R, Smith WS, Young WL, Saloner D (2009) Phase-contrast magnetic resonance imaging measurements in intracranial aneurysms in vivo of flow patterns, velocity fields, and wall shear stress: comparison with computational fluid dynamics. Magn Reson Med 61(2):409–417. https://doi.org/10.1002/mrm.21861
23. Boccadifuoco A, Mariotti A, Capellini K, Celi S, Salvetti MV (2018) Validation of numerical simulations of thoracic aorta hemodynamics: comparison with in vivo measurements and stochastic sensitivity analysis. Cardiovasc Eng Tech 9(4):688–706. https://doi.org/10.1007/s13239-018-00387-x
24. Miyazaki S, Itatani K, Furusawa T, Nishino T, Sugiyama M, Takehara Y, Yasukochi S (2017) Validation of numerical simulation methods in aortic arch using 4D flow MRI. Heart Vessels 32:1032–1044. https://doi.org/10.1007/s00380-017-0979-2
25. Cibis M, Potters WV, Gijsen FJH, Marquering H, vanBavel E, van der Steen AFW, Nederveen AJ, Wentzel JJ (2014) Wall shear stress calculations based on 3D cine phase contrast MRI and computational fluid dynamics: a comparison study in healthy carotid arteries. NMR Biomed 27:826–834. https://doi.org/10.1002/nbm.3126
26. Wentland AL, Grist TM, Wieben O (2013) Repeatability and internal consistency of abdominal 2D and 4D phase contrast MR flow measurements. Acad Radiol 20(6):699–704. https://doi.org/10.1016/j.acra.2012.12.019
27. Ebel S, Hübner L, Köhler B, Kropf S, Preim B, Jung B, Grothoff M, Gutberlet M (2019) Validation of two accelerated 4D flow MRI sequences at 3 T: a phantom study. Eur Radiol Exp 3(1):1–12. https://doi.org/10.1186/s41747-019-0089-2
28. Park J, Kim J, Chang Y, Youn SW, Lee HJ, Kang EJ, Lee KN, Suchánek V, Hyun S, Lee J (2019) Analysis of the time-velocity curve in phase-contrast magnetic resonance imaging: a phantom study. Comput Assist Surg 24:3–12. https://doi.org/10.1080/24699322.2019.1649066
29. Kim GB, Lee S, Kim H, Yang DH, Kim Y-H, Kyung YS, Kim C-S, Choi SH, Kim BJ, Ha H, Kwon SU, Kim N (2016) Three-dimensional printing: basic principles and applications in medicine and radiology. Korean J Radiol 17(2):182–197. https://doi.org/10.3348/kjr.2016.17.2.182
30. Chung TG, Kim YS, Chang Y, Lee SK, Kim YH, Ryeom HK, Lee JM, Lee CH, Kim TH, Suh KJ (2000) High signal intensity on T1-weighted MR image related to vacuum cleft in the intervertebral disk: clinical and phantom study. J Korean Radiol Soc 43:651–656. https://doi.org/10.3348/jkrs.2000.43.6.651
31. Segur JB, Oberstar HE (1951) Viscosity of glycerol and its aqueous solutions. Ind Eng Chem 43(9):2117–2120. https://doi.org/10.1021/ie50501a040
32. Volk A, Kähler CJ (2018) Density model for aqueous glycerol solutions. Exp Fluids 59(5):75. https://doi.org/10.1007/s00348-018-2527-y
33. Lotz J, Meier C, Leppert A, Galanski M (2002) Cardiovascular flow measurement with phase-contrast MR imaging: basic facts and implementation. Radiographics 22(3):651–671. https://doi.org/10.1148/radiographics.22.3.g02ma11651
34. Rosner B (2015) Fundamentals of biostatistics. Brookes/Cole, USA
35. Chandran KB, Rittgers SE, Yoganathan AP (2012) Biofluid mechanics: the human circulation. CRC Press, USA
36. Rajan KS, Pitchumani B, Srivastava SN, Mohanty B (2007) Two-dimensional simulation of gas–solid heat transfer in pneumatic conveying. Int J Heat Mass Transf 50(5–6):967–976. https://doi.org/10.1016/j.ijheatmasstransfer.2006.08.009
37. Frydrychowicz A, François CJ, Turski PA (2011) Four-dimensional phase contrast magnetic resonance angiography: potential clinical applications. Eur J Rad 80:24–35. https://doi.org/10.1016/j.ejrad.2011.01.094
38. van Ooij P, Schneiders JJ, Marquering HH, Majoie CB, van Bavel E, Nederveen AJ (2013) 3D cine phase-contrast MRI at 3T in intracranial aneurysms compared with patient-specific computational fluid dynamics. Am J Neurorad 34(9):1785–1791. https://doi.org/10.3174/ajnr.A3484
39. Ha H, Lantz J, Haraldsson H, Casas B, Ziegler M, Karlsson M, Saloner D, Dyverfelt P, Ebbers T (2016) Assessment of turbulent viscous stress using ICOSA 4D flow MRI for prediction of

hemodynamic blood damage. Sci Rep 6:39773. https://doi.org/10.1038/srep39773
40. Lantz J, Ebbers T, Engvall J, Karlsson M (2013) Numerical and experimental assessment of turbulent kinetic energy in an aortic coarctation. J Biomech 46(11):1851–1858. https://doi.org/10.1016/j.jbiomech.2013.04.028
41. Ngo MT, Kim CI, Jung J, Chung GH, Lee DH, Kwak HS (2019) Four-dimensional flow magnetic resonance imaging for assessment of velocity magnitudes and flow patterns in the human carotid artery bifurcation: comparison with computational fluid dynamics. Diagnostics 9(4):223. https://doi.org/10.3390/diagnostics9040223
42. Kweon J, Yang DH, Kim GB, Kim N, Paek M, Stalder AF, Greiser A, Kim Y-H (2016) Four-dimensional flow MRI for evaluation of post-stenotic turbulent flow in a phantom: comparison with flowmeter and computational fluid dynamics. Eur Radiol 26(10):3588–3597. https://doi.org/10.1007/s00330-015-4181-6
43. Dyverfeldt P, Kvitting JPE, Sigfridsson A, Engvall J, Bolger AF, Ebbers T (2008) Assessment of fluctuating velocities in disturbed cardiovascular blood flow: in vivo feasibility of generalized phase-contrast MRI. J Magn Reson Imaging 28(3):655–663. https://doi.org/10.1002/jmri.21475
44. Box FM, van der Geest RJ, van der Grond J, van Osch MJ, Zwinderman AH, Palm-Meinders IH, Reiber JH (2007) Reproducibility of wall shear stress assessment with the paraboloid method in the internal carotid artery with velocity encoded MRI in healthy young individuals. J Magn Reson Imaging 26(3):598–605. https://doi.org/10.1002/jmri.21086
45. Dyverfeldt P, Bissell M, Barker AJ, Bolger AF, Carlhäll CJ, Ebbers T, Markl M (2015) 4D flow cardiovascular magnetic resonance consensus statement. J Cardiovas Magn Reson 17(1):1–19. https://doi.org/10.1186/s12968-015-0174-5